Ultrahigh resolution spectral-domain optical coherence tomography using the 1000–1600 nm spectral band: supplement

LIANE BERNSTEIN,[1,2] ○iD ANTOINE RAMIER,[1,3] ○iD JIAMIN WU,[1,4,5] ○iD VERA D. AIELLO,[6] MARIE J. BÉLAND,[7] CHARLES P. LIN,[1,8] AND SEOK-HYUN YUN[1,3,8,*]

[1]Wellman Center for Photomedicine, Massachusetts General Hospital, 50 Blossom Street, Boston, MA 02140, USA
[2]Department of Electrical Engineering and Computer Science, Massachusetts Institute of Technology, Cambridge, MA, USA
[3]Health Sciences and Technology, Massachusetts Institute of Technology, Cambridge, MA, USA
[4]Department of Automation, Tsinghua University, Beijing 100084, China
[5]Institute for Brain and Cognitive Science, Tsinghua University, Beijing 100084, China
[6]Laboratory of Pathology, Heart Institute, University of São Paulo Medical School, São Paulo, Brazil
[7]Division of Pediatric Cardiology, The Montreal Children's Hospital of the McGill University Health Centre, Montréal, Quebec, Canada
[8]Department of Dermatology, Harvard Medical School, Boston, MA, USA
*syun@mgh.harvard.edu

Ultrahigh resolution spectral-domain optical coherence tomography using the 1000-1600 nm spectral band: supplemental document

1. UHR-SD-OCT system parameters

1.1 Axial resolution

The axial resolution of an OCT system is directly related to the central wavelength and bandwidth of its source. In fact, the axial resolution is set by the width of the Fourier transform of the detected source spectrum (with the z axis rescaled by a factor of 2 to account for light travelling twice through the sample), i.e., the FWHM of the coherence envelope. If the source is Gaussian of spectral width $|k_2 - k_1|$ (FWHM), the corresponding coherence envelope is also Gaussian, and the axial resolution is [1,2]:

$$\delta z = \frac{2\ln(2)}{\pi n} \frac{\lambda_1 \lambda_2}{|\lambda_2 - \lambda_1|} \tag{S1}$$

with $\lambda_1 = 2\pi/k_1$, $\lambda_2 = 2\pi/k_2$, and n the refractive index. For $\lambda_1 = 1.0$ μm and $\lambda_2 = 1.6$ μm, the theoretical axial resolution is $\delta z = 1.2$ μm. The reason UHR-OCT systems typically use shorter-wavelength sources is clear: δz scales with $\lambda_1 \lambda_2$. Conversely, a UHR-OCT system at longer wavelengths has increased complexity from the limited availability of sources, detectors, and from the challenges related to management of chromatic aberration with a large bandwidth. It should be noted that our source spectrum is not Gaussian; therefore, we normalize received data by the source spectrum for numerical spectral flattening (see section 3 below for full data processing). Furthermore, we employ windowing to reduce sidelobes and improve sensitivity at the expense of resolution (see section 5 below for corresponding theory and measurements of resolution and sensitivity). However, the scaling ideas presented above still hold: a system operating at a shorter central wavelength and larger bandwidth will have improved axial resolution.

1.2 Lateral resolution

The lateral resolution of an OCT system depends on the numerical aperture of the objective lens (as in histology). The lateral spot size of the laser on the sample ($2w_0 = 1/e^2$ spot diameter) can be calculated from Gaussian optics, assuming a perfect lens [3]:

$$2w_0 = \frac{4\lambda f}{\pi d} \tag{S2}$$

where λ is the wavelength, f is the focal length of the lens, d is the beam size on the back aperture of the objective ($1/e^2$ diameter), and where the numerical aperture can be approximated as NA $= d/(2f)$ in air. Using equation S2, in our system, the lateral FWHM ($= \sqrt{2\ln2}\, w_0$) is approximately 15 μm (confirmed with a USAF 1951 resolution target).

1.3 Maximum imaging depth

The maximum imaging depth in OCT is affected by several distinct parameters. A first consideration is the depth of focus (DOF), which is defined as the axial distance over which the beam size doubles in diameter from its smallest point (focal spot). The axial DOF is given by equation S3 [4], and can be directly related to lateral spot size:

$$\text{DOF} = \frac{8\lambda f^2}{\pi d^2} = \frac{2\pi}{\lambda} w_0^2 \tag{S3}$$

Thus, we note the compromise between lateral resolution and DOF; as lateral resolution is improved, imaging depth is reduced, since a more tightly focused beam diverges faster. If the beam has diverged too much, there will not be sufficient light returning to the spectrometer to observe a signal. In our system, DOF = 0.78 mm.

Secondly, tissue penetration depth is the maximum depth in a sample at which an OCT signal can be observed, which depends on sample absorption and scattering properties. These properties are related to source wavelength, where scattering tends to decrease in tissue with longer wavelengths in the infrared, especially with respect to visible wavelengths [5–7].

Another factor affecting OCT imaging depth is sensitivity, which is the smallest signal that can be observed with respect to incident power on the sample, and is usually expressed in decibels (dB). It is limited by the noise sources in the system, notably detector noise (thermal noise), laser relative intensity noise (RIN) and shot noise [8]. When using supercontinuum sources for OCT to achieve a broad spectral bandwidth, the RIN tends to be the most important source of noise [9].

Next, the imaging range ($z_{\max}$) is related to the finite spectral sampling of the spectrometer, and represents the axial depth that can be imaged in one spectrometer acquisition [1]:

$$z_{\max} = \frac{n\lambda_0^2}{4\Delta\lambda} \tag{S4}$$

where $\Delta\lambda$ is the wavelength spacing between pixels of the spectrometer. In our system, $z_{\max}$ = 1.4 mm in air. This range can be doubled by implementing "full-range OCT", as described in Refs. [1,7,10,11].

Lastly, the signal-to-noise ratio (SNR) falls off with depth due to "roll-off", where $R(\Delta z)$ gives the envelope of the decay with respect to depth (Δz) and is theoretically expressed by [12]:

$$R(\Delta z) = \text{sinc}^2\left(\frac{\pi\Delta z}{2\alpha}\right)\exp\left(-\frac{\pi^2 r^2 (\Delta z)^2}{8\alpha^2\ln(2)}\right) \tag{S5}$$

with $r = \delta\lambda/\Delta\lambda$ and $\alpha = \lambda_0^2/(4\Delta\lambda)$, where $\Delta\lambda$ is the wavelength spacing between pixels, $\delta\lambda$ is the spectrometer resolution, and λ_0 is the center wavelength. To calculate $\delta\lambda$, we look at a diffraction-limited spot produced on the camera by a single wavelength λ_a, and determine the wavelength λ_b that would be one spot FWHM away on the camera. Then, $\delta\lambda = \lambda_b - \lambda_a$. Our spectrometer design aimed to match $\delta\lambda$ to $\Delta\lambda$, where one spot size diameter on the camera would equal the size of a pixel (10 μm). The theoretical r for our system is therefore $r = 1$, however, $r = 1.52$ was found to better match the experimental data. This discrepancy is likely the result of slight misalignment in the spectrometer.

2. Spectrometer design

Proper spectrometer design is critical toward achieving good sensitivity over a large depth (low roll-off and signal loss). To minimize aberrations and for ease of alignment, we chose a grating with a small spatial frequency of 600 lines/mm (Wasatch Photonics WP-600/1550-25.4, angle of incidence (AOI) θ_i = -27.7°) for use with long focal length lenses. The grating equation (S6) illustrates that a small spatial frequency reduces the transmission angle and thus allows the use of longer focal length lenses:

$$\sin\theta_t - \sin\theta_i = l \cdot m \cdot \lambda \tag{S6}$$

where θ_t is the transmitted angle, θ_i is the grating AOI, l is the spatial frequency of the grating (lines per millimeter) and m is the order. In our spectrometer, we use the first order, checking that the second order does not overlap for any wavelength used. To determine the required lens focal lengths, we maximized the detected bandwidth ($\lambda_2 - \lambda_1$), centered at 1.3 μm, while satisfying the constraints outlined below. The linescan camera (GL2048R, Sensors Unlimited)

has 2048 pixels of size 10 μm (pitch) by 210 μm (height). Therefore, the reddest and bluest wavelengths are separated by 20.47 mm on the camera (equation S7). Furthermore, the spot size of a monochromatic source on the camera should be <10 μm to minimize roll-off. Since the input fiber to the spectrometer has a mode field diameter (MFD) of 6 μm across the entire bandwidth, collimating and focusing lenses of equal focal lengths ($f_{col} = f_{focus} = f$) satisfy this condition. We also wanted to select this focal length f such that the beam of width d is not clipped on the 1-inch grating (equation S8) or the 2-inch focusing optics (equation S9). These constraints can be summarized as follows:

$$\frac{20.47 \text{ mm}}{2} = f \cdot \tan\left(\frac{\theta_2 - \theta_1}{2}\right) \tag{S7}$$

$$\frac{2 \cdot \lambda_2 \cdot f}{\pi \cdot 6 \text{ μm}} < \frac{25.4 \text{ mm}}{2} \cdot \cos(27.7°) \tag{S8}$$

$$\frac{20.47 \text{ mm}}{2} + \frac{2 \cdot \lambda_2 \cdot f}{\pi \cdot 6 \text{ μm}} < \frac{50.8 \text{ mm}}{2} \tag{S9}$$

with the variables defined in the spectrometer schematic in Fig. S1. Collimating and focusing optics with 50 mm focal lengths satisfy these constraints, with $\lambda_1 = 985$ nm and $\lambda_2 = 1615$ nm.
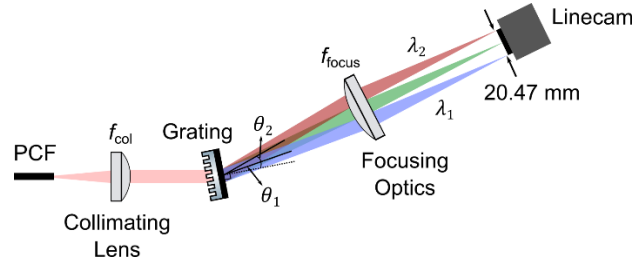

Fig. S1. Spectrometer parameters.

To design the spectrometer focusing optics with off-the-shelf lenses over our broad wavelength band, we minimized chromatic as well as geometric aberrations with Zemax® ray-tracing software. First, a perfect grating was inserted into the simulation, then a cemented achromat (Thorlabs AC508-080-C) with a slightly longer focal length than the desired focal length (used: $f = 80$ mm; desired: $f = 50$ mm). N-BK7 lenses were then added before and after the cemented achromat with variable distances and radii of curvature. A generic merit function was applied, minimizing the RMS spot size along the camera line dimension (y). The design was not diffraction-limited after optimization, and therefore, another degree of freedom was added: lateral translation of the source and grating. The final design shown in Fig. S2 includes a plano-convex lens with $f = 150$ mm (Thorlabs LA1417-C), the cemented achromat with $f = 80$ mm, and a positive meniscus lens with $f = 150$ mm (Thorlabs LE1418-C).
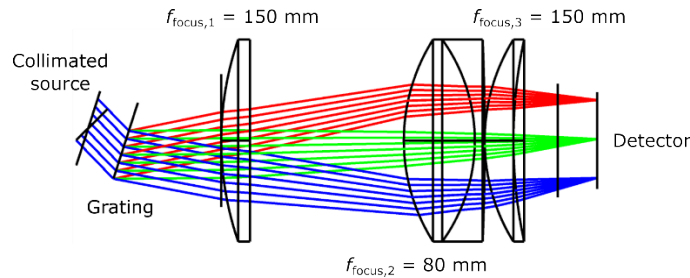

Fig. S2. Final spectrometer focusing optics, simulated and optimized in Zemax®

The RMS spot diameter (simulated by Zemax®) is shown Fig. S3 and is compared with a simple pair of $f = 100$ mm cemented achromats (Thorlabs AC508-100-C). With the pair of achromats, aberrations dominate and cause the spot size along the camera axis (y) to be larger than 10 µm over most of the desired spectral band. Perpendicular to the camera axis, in both cases, the spot size remains well below the camera pixel height.
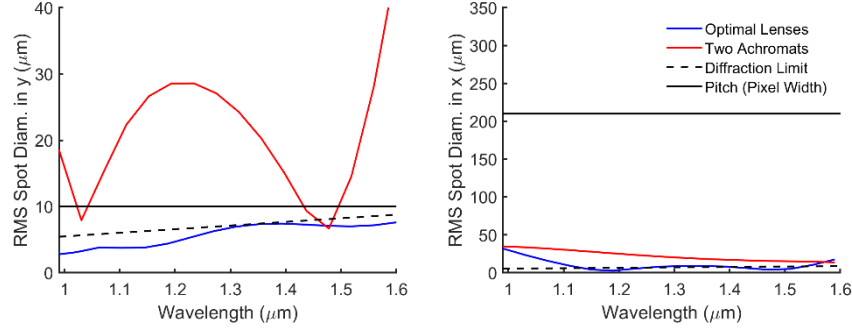

Fig. S3. Simulated focused spot diameters in our spectrometer using Zemax® ray tracing. Comparison of our optimized design with two cemented achromats, the diffraction limit, and the camera pixel size. (Left) along camera axis. (Right) perpendicular to camera axis.

3. Image processing

The raw signal received on the line camera is:

$$I_{\det}(k) = \frac{1}{4}\, I_{\text{source}}(k)\big(1 + r_s + 2\sqrt{r_s}\cos(2k\Delta z + \varphi(k))\big) \qquad (S10)$$

where $I_{\text{source}}(k)$ is the source spectrum, $k = 2\pi/\lambda$ is the wavenumber, r_s is the sample reflectivity, Δz is the sample depth (optical path length difference between the sample and reference arms) and $\varphi(k)$ is the dispersion mismatch between the sample and reference arms. The processing steps from the acquired raw spectra to images are:

- Background subtraction;
- Envelope normalization (dividing by the source spectrum acquired from the reference arm);
- k-mapping (on the camera, the signal is linear in wavelength λ, but it must be resampled to be linear in $k = 2\pi/\lambda$);
- Numerical dispersion compensation;
- Windowing;
- Fourier transform ($k \rightarrow z$);
- z-scaling to assign delay values in µm.

In more detail, first, calibration was performed by placing a mirror in the sample position and interferograms were acquired at 50 µm displacements of the reference mirror. For the initial calibration step, 2,000 interferograms were acquired and averaged per mirror position to ensure accurate mapping, but no such time-averaging was performed in the system characterization acquisitions. 2,000 reference spectra were recorded and averaged with the sample arm blocked. The averaged reference spectrum was subtracted from the interferograms, and then the interferograms were divided by the reference spectrum for numerical spectral flattening, i.e., envelope normalization.

k-mapping was achieved by taking the difference of the phase of the Hilbert transform of consecutive interferograms, yielding $2k\Delta z_{i+1} - 2k\Delta z_i$, where i represents each of the mirror positions. This difference phase was fitted with the sum of a hyperbola representing the wavelength-to-wavenumber conversion and a third-order polynomial to partially account for aberrations. k-mapping of each interferogram was then performed by cubic spline interpolation.

Dispersion compensation was implemented similarly to Refs. [13,14], where the phase of the Hilbert transform of the interferogram (now mapped to wavenumber) yields $2k\Delta z + \varphi(k)$. This curve was fitted with a seventh-order polynomial, where the first order represents the desired signal and the higher order terms represent the dispersion. The dispersion can then be compensated by multiplying the interferogram by an inverse phase term.

Next, the interferogram was windowed to reduce sidelobes at the expense of resolution [15] with a half-Blackman, half-Hamming window (see section 5 below). The corrected interferogram was then Fourier transformed to yield an A-line using a fast Fourier transform with 2^{14} points. Lastly, the A-line was z-scaled with a linear fit, assuming a 50 µm translation between each interferogram and squared to calculate the reflectivity profile (but not to calculate resolution).

To process data after this calibration, we performed background subtraction and normalization, then simply applied the saved k-mapping, dispersion compensation, windowing, Fourier transform and z-scaling for each A-line.

4. Power level on sample

Table S1. Maximum Permissible Exposure (MPE), Rule 1

Wavelength (nm)	$1000 \leq \lambda \leq 1050$	$1050 \leq \lambda \leq 1400$	$1400 \leq \lambda \leq 1500$	$1500 \leq \lambda \leq 1600$
MPE[a] (J/cm^2)	$2.0\,C_A \times 10^{-2} = .080$	$2.0\,C_A \times 10^{-2} = .10$	0.3	1.0
MPE[b] (µJ/spot)	0.42	0.53	1.6	5.3
Energy fraction[c]	0.01	0.60	0.20	0.19
Energy (µJ)[d]	3.1×10^{-6}	1.9×10^{-4}	6.3×10^{-5}	5.9×10^{-5}
Energy/MPE	7.4×10^{-6}	3.5×10^{-4}	3.9×10^{-5}	1.1×10^{-5}
$\sum$ Energy/MPE	0.00041			

[a]$C_A = 10^{0.002(\lambda-700)}$ for $1000 \leq \lambda \leq 1050$; in the worst case, with $\lambda = 1000$ nm, $C_A = 4.0$.
$C_A = 5.0$ for $1050 \leq \lambda \leq 1400$.
[b]MPE per focal spot is MPE in J/cm^2 multiplied by the spot area (π (0.0013 cm)$^2 = 5.3 \times 10^{-6}$ cm^2), where 0.0013 cm is the $1/e^2$ beam radius at the focal spot.
[c]Fraction of total energy in this wavelength band (integral over different regions of Fig. 2a in main text).
[d]Energy in one pulse (0.025 W/(80 × 10^6 Hz) = 3.1×10^{-10} J) multiplied by energy fraction.

Table S2. Maximum Permissible Exposure (MPE), Rule 2

Wavelength (nm)	$1000 \leq \lambda \leq 1050$	$1050 \leq \lambda \leq 1400$	$1400 \leq \lambda \leq 1500$	$1500 \leq \lambda \leq 1600$
MPE[a] (J/cm^2)	$1.1\,C_A \times t^{0.25} = 0.44$	$1.1\,C_A \times t^{0.25} = 0.55$	0.3	1.0
MPE[b] (µJ/spot)	2.3	2.9	1.6	5.3
Power fraction[c]	0.01	0.60	0.20	0.19
Power (mW)[d]	0.25	15	5.0	4.8
Energy (µJ)[e]	.025	1.5	0.50	.48
Energy/MPE	.011	0.51	0.31	0.089
$\sum$ Energy/MPE	0.93			

[a]$C_A = 10^{0.002(\lambda-700)}$ for $1000 \leq \lambda \leq 1050$; in the worst case, with $\lambda = 1000$ nm, $C_A = 4.0$.
$C_A = 5.0$ for $1050 \leq \lambda \leq 1400$. t is the acquisition time for one A-line (10^{-4} s).
[b]MPE per focal spot is MPE in J/cm^2 multiplied by the spot area (π (0.0013 cm)$^2 = 5.3 \times 10^{-6}$ cm^2), where 0.0013 cm is the $1/e^2$ beam radius at the focal spot.
[c]Fraction of total power in this wavelength band (integral over different regions of Fig. 2a in main text).
[d]25 mW multiplied by power fraction.
[e]Power multiplied by exposure time (10^{-4} s).

To determine the safety limits to laser power on the sample, we refer to the maximum permissible exposure (MPE) listed in the American National Standard for Safe Use of Lasers (ANSI Z136.1), Tables 7b and 7c, on pages 87 and 88, respectively [16]. The two ANSI Rules that apply to non-ocular (i.e., "skin") exposure are: "Exposure of the skin shall not exceed the MPE based upon a single-pulse exposure (Rule 1), and the average irradiance of the pulse train shall not exceed the MPE applicable for the total pulse train, duration T (Rule 2)" (p. 68). Furthermore, when multiple wavelength bands are used, "the MPE must first be determined for each wavelength separately. Exposures from several wavelengths are additive on a proportional

basis of spectral effectiveness" (p. 64). Mathematically, the sum of the ratios of exposures Q to MPEs (both energies in units of Joules) over each wavelength band i must be less than 1 [17]:

$$\sum_i \frac{Q_i}{MPE_i} < 1 \qquad (S11)$$

The MPE calculations for a single pulse (Rule 1) and a single A-line (Rule 2) are given in Tables S1 and S2, respectively. The final row of each Table shows that the constraint outlined in equation S11 is satisfied. We note, however, that the MPE could be exceeded by Rule 2 in our system in certain scenarios. Firstly, the MPE is given in the ANSI standard for uniform illumination across an aperture, not a Gaussian beam. Secondly, the beam may be kept fixed on a certain spot for alignment or if there is a desire to average many consecutive A-lines, increasing the effective exposure time. The beam may also be more tightly confined with a higher NA objective for improved lateral resolution. Therefore, in a clinical setting, it may be desirable to lower the power in the sample arm, or to operate the system at a faster A-line rate for lower energy accumulation per spot. This decrease in sample illumination power will not necessarily degrade image quality; as proposed in the main text, the sensitivity can be improved by up to ~10 dB using sources with lower relative intensity noise.

5. Windowing: trade-off of sensitivity versus axial resolution

As mentioned in section 1 above, the theoretical axial resolution in OCT is given by the envelope of the Fourier transform of the source spectrum. A basic example is shown in Fig. S4. A theoretical Gaussian spectrum (in k space, solid curve in Fig. S4a) of FWHM = $|2\pi/\lambda_1-2\pi/\lambda_2|$ with $\lambda_1 = 1.0$ μm and $\lambda_2 = 1.6$ μm is processed by a Fast Fourier Transform (FFT) to yield a point spread function (PSF) that is a Gaussian of FWHM $\delta z = 1.2$ μm, as predicted by equation S1. However, in a real OCT system with a finite number of spectrometer pixels to acquire the signal, the source spectrum is effectively multiplied by a rectangular window of width $|2\pi/\lambda_1-2\pi/\lambda_2|$. Furthermore, in our experiments, we numerically flatten the envelope of the signal by dividing it by the source spectrum. Therefore, our processed spectrum is theoretically shaped like a rectangular window (dashed curve in Fig. S4a). The ensuing PSF obtained by FFT is a sinc function, with a wider PSF of FWHM 1.6 μm, along with sidelobes (dashed curve in Fig. S4b). To reduce the presence of these sidelobes and improve sensitivity, the interferograms in k space can be multiplied by a window function.
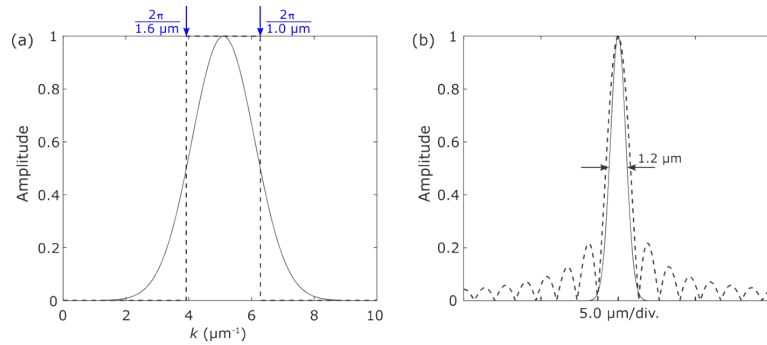

Fig. S4. (a) Normalized theoretical Gaussian source spectrum of FWHM = $|2\pi/\lambda_1-2\pi/\lambda_2|$ with $\lambda_1 = 1.0$ μm and $\lambda_2 = 1.6$ μm (solid curve). The dashed curve shows a rectangular window of width equal to the Gaussian FWHM. (b) Absolute value of the FFT of the two curves shown in (a). Illustrated FWHM of 1.2 μm is for Gaussian; FWHM obtained for rectangular window is 1.6 μm.
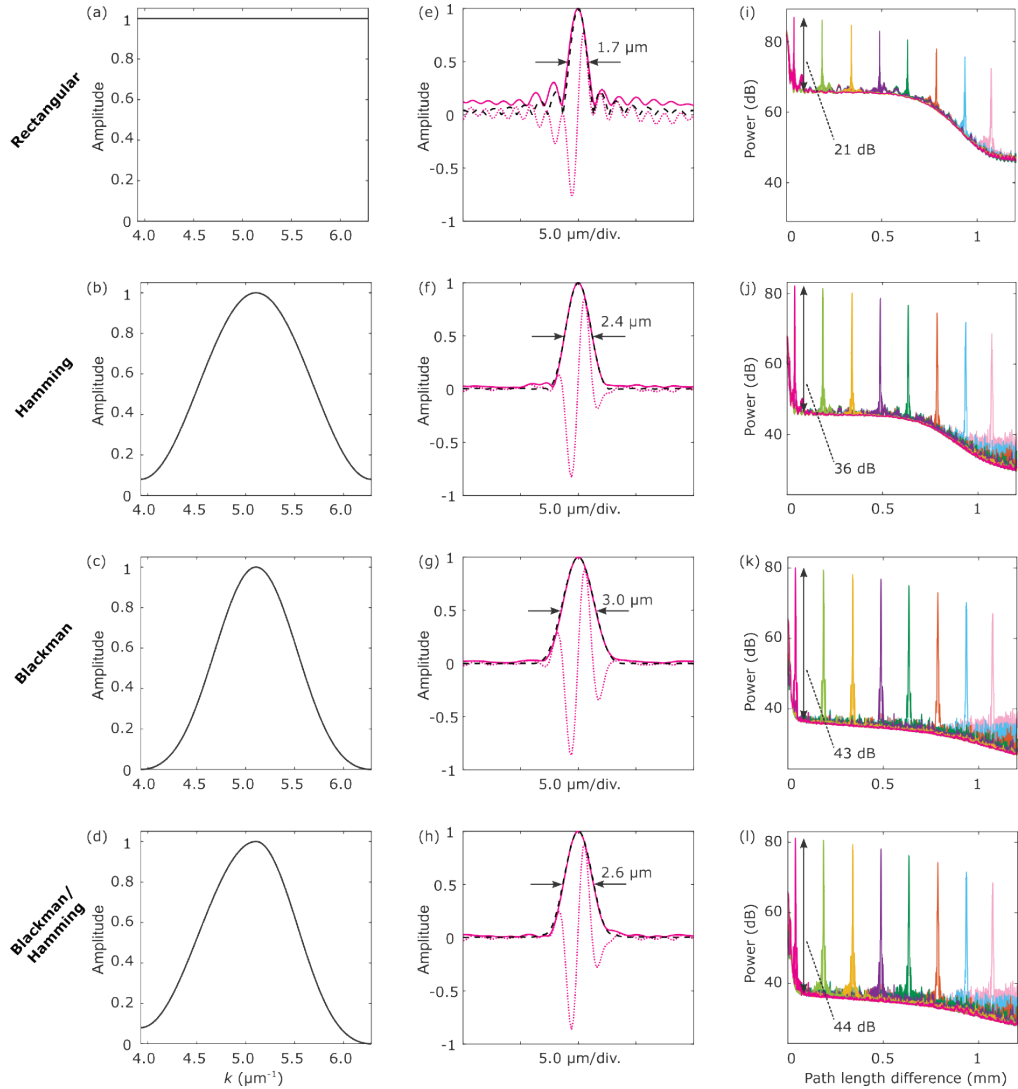
Fig. S5. Effects of windowing on point spread functions of a -60 dB reflector. Measurement procedure is as described in main text, section 2 and Fig. 3, and processing is discussed in section 3 above. (a-d) Different applied windows to the interferograms before Fourier transforming. Outside of the range shown, the amplitude is null with zero padding of the FFT. (e-h) Point spread functions at a delay of 40 μm, where axial resolution is defined as the FWHM of the coherence envelope. Dashed black curves are the theoretical resolution limits of each applied window (FFT of window), dotted pink curve is the real part of the measured PSF and solid pink curve is the absolute value of the measured PSF. (i-l) Sensitivity curves illustrating SNR from reflectivity profiles.

As stated in section 3 above, we multiplied acquired interferograms by a window function before Fourier transforming to improve sensitivity at the expense of axial resolution. The theoretical PSF is then simply the Fourier transform of the window function. Figure S5 shows our axial resolution and sensitivity measurements for different applied windows. Since the signal is weaker for shorter wavelengths, the SNR is lower; therefore, the Blackman window improves the sensitivity by reducing the weighting of shorter wavelengths. In fact, we found a significant increase in the noise floor (~7 dB) at 10 klps by using a full Hamming window compared with a Blackman window. However, resolution is worsened with the Blackman

window as it decreases the effective source bandwidth. At longer wavelengths, the signal strength remains high, therefore, we opted for a half-Blackman, half-Hamming window as a compromise between reducing sidelobes and maintaining axial resolution. Note that we also experimented with applying an additional narrow window to suppress the pump peak at 1064 nm, but found that this step did not have a significant effect on the results.

6. Location of cardiac imaging

Figure S6 shows a photo of the laser spot on the membranous septum of the pig heart during UHR-SD-OCT imaging (the longpass filter was removed from the supercontinuum output to observe the laser position on the sample).
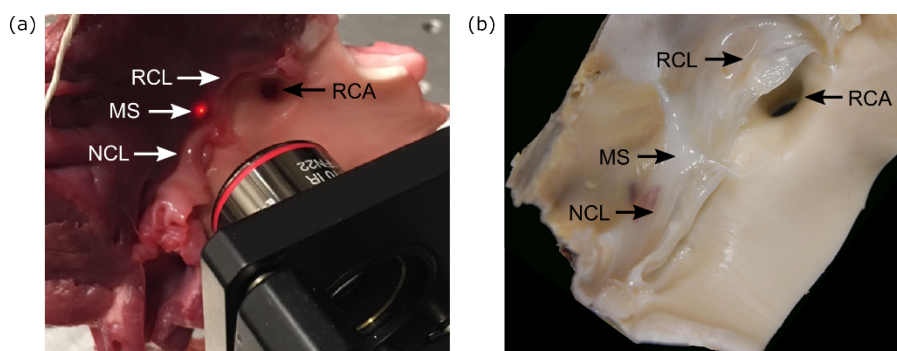

Fig. S6. Imaging location of membranous septum (MS) of pig heart. (a) Laser spot on the MS between the semilunar lines of attachment of the right coronary leaflet (RCL) and the non-coronary leaflet (NCL) of the aortic valve. The MS was located via trans-illumination from the right side of the heart. For visualization of the laser spot on the sample, the 980 nm longpass filter was removed from the UHR-OCT setup to transmit visible light from the supercontinuum source. RCA: right coronary artery. (b) A section of a pig's heart after formalin fixation. The area of the membranous septum (MS) was located as described in the fresh specimen.

References

1. W. Drexler and J. G. Fujimoto, eds., *Optical Coherence Tomography* (Springer International Publishing, 2015).
2. A. F. Fercher, W. Drexler, C. K. Hitzenberger, and T. Lasser, "Optical coherence tomography—principles and applications," Reports on Progress in Physics **66**, 239–303 (2003).
3. H. A. Haus, *Waves and Fields in Optoelectronics* (Prentice-Hall, 1984).
4. B. E. A. Saleh and M. C. Teich, *Fundamentals of Photonics*, Second Edition (John Wiley & Sons, 2007).
5. S. L. Jacques, "Optical properties of biological tissues: a review," Phys. Med. Biol. **58**, R37 (2013).
6. J. M. Schmitt, A. Knuttel, M. Yadlowsky, and M. A. Eckhaus, "Optical-coherence tomography of a dense tissue: statistics of attenuation and backscattering," Phys. Med. Biol. **39**, 1705 (1994).
7. N. Nishizawa, H. Kawagoe, M. Yamanaka, M. Matsushima, K. Mori, and T. Kawabe, "Wavelength Dependence of Ultrahigh-Resolution Optical Coherence Tomography Using Supercontinuum for Biomedical Imaging," IEEE J. Select. Topics Quantum Electron. **25**, 1–15 (2019).
8. S. H. Yun, G. J. Tearney, J. F. de Boer, N. Iftimia, and B. E. Bouma, "High-speed optical frequency-domain imaging," Opt. Express **11**, 2953–2963 (2003).
9. M. Jensen, I. B. Gonzalo, R. D. Engelsholm, M. Maria, N. M. Israelsen, A. Podoleanu, and O. Bang, "Noise of supercontinuum sources in spectral domain optical coherence tomography," J. Opt. Soc. Am. B **36**, A154 (2019).
10. M. Wojtkowski, A. Kowalczyk, R. Leitgeb, and A. F. Fercher, "Full range complex spectral optical coherence tomography technique in eye imaging," Opt. Lett. **27**, 1415–1417 (2002).
11. Y. Yasuno, S. Makita, T. Endo, G. Aoki, M. Itoh, and T. Yatagai, "Simultaneous B-M-mode scanning method for real-time full-range Fourier domain optical coherence tomography," Appl. Opt. **45**, 1861–1865 (2006).
12. S. H. Yun, G. J. Tearney, B. E. Bouma, B. H. Park, and J. F. de Boer, "High-speed spectral-domain optical coherence tomography at 1.3 μm wavelength," Opt. Express **11**, 3598–3604 (2003).
13. B. Cense, N. A. Nassif, T. C. Chen, M. C. Pierce, S.-H. Yun, B. H. Park, B. E. Bouma, G. J. Tearney, and J. F. de Boer, "Ultrahigh-resolution high-speed retinal imaging using spectral-domain optical coherence tomography," Opt. Express **12**, 2435 (2004).

14.   M. Wojtkowski, V. J. Srinivasan, T. H. Ko, J. G. Fujimoto, A. Kowalczyk, and J. S. Duker, "Ultrahigh-resolution, high-speed, Fourier domain optical coherence tomography and methods for dispersion compensation," Opt. Express **12**, 2404–2422 (2004).
15.   F. J. Harris, "On the use of windows for harmonic analysis with the discrete Fourier transform," Proceedings of the IEEE **66**, 51–83 (1978).
16.   Laser Institute of America, *American National Standard for Safe Use of Lasers*, ANSI Z136.1 (2014).
17.   T.L. Lyon, "Hazard Analysis Technique for Multiple Wavelength Lasers," Health Physics **49**, 221–226 (1985).